

www.acsami.org Research Article

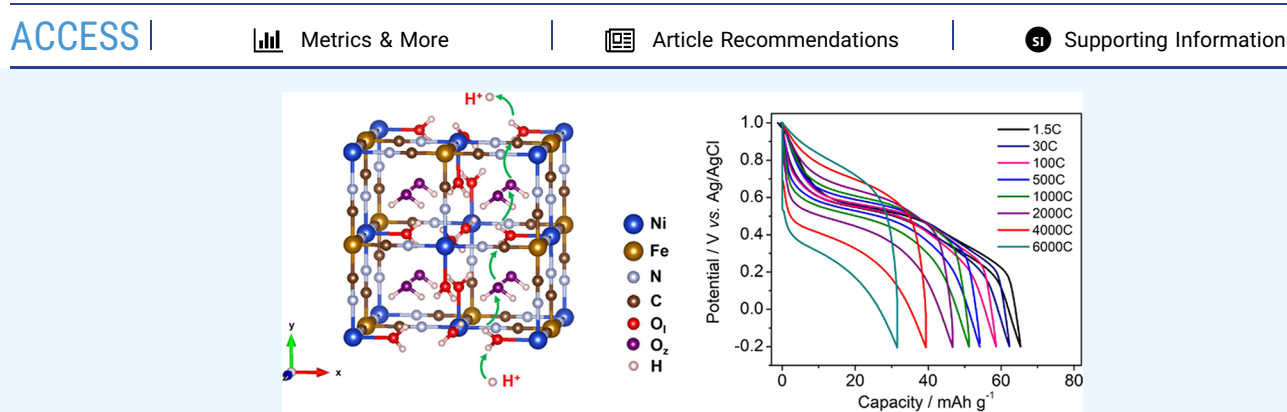
# Hydrous Nickel-Iron Turnbull's Blue as a High-Rate and Low-Temperature Proton Electrode

Xianyong Wu, Shen Qiu, Yunkai Xu, Lu Ma, Xuanxuan Bi, Yifei Yuan, Tianpin Wu, Reza Shahbazian-Yassar, Jun Lu,\* and Xiulei Ji\*



Cite This: ACS Appl. Mater. Interfaces 2020, 12, 9201–9208





ABSTRACT: Proton batteries are emerging as a promising solution for energy storage; however, their development has been hindered by the lack of suitable cathode materials. Herein, a hydrous Turnbull's blue analogue (TBA) of Ni[Fe(CN)<sub>6</sub>]<sub>2/3</sub>·4H<sub>2</sub>O has been investigated as a viable proton cathode. Particularly, it shows an extremely high rate performance up to 6000 C (390 A g<sup>-1</sup>) at room temperature and delivers good capacity values at a low temperature of -40 °C in an aqueous electrolyte. The excellent rate capability is also amenable to high mass loadings of 10 mg cm<sup>-2</sup>. Such fast and low-temperature rate behavior likely stems from the fast proton conduction that is afforded by the Grotthuss mechanism inside the TBA structure. Furthermore, advanced characterization, including in operando synchrotron X-ray diffraction (XRD), and X-ray absorption near-edge structure (XANES) were employed to understand the changes of crystal structures and the oxidation-states of metal elements of the electrodes.

KEYWORDS: proton insertion, Turnbull's blue analogues, Grotthuss mechanism, high rate, low temperature

# **■** INTRODUCTION

The ever-increasing demand for the storage of renewable energy entails the development of next-generation post-lithium batteries. Let Currently, alternative metal cations such as Na<sup>+</sup>, K<sup>+</sup>, Mg<sup>2+</sup>, Al<sup>3+</sup>, and Zn<sup>2+</sup>, represent prominent charge carriers for alternative batteries; however, little attention has been devoted to nonmetal cations such as proton and ammonium, albeit their distinct properties may potentially transform the electrochemical performance of electrodes. Page 11

Recently, the interests on protons have been revived as an intriguing ionic charge carrier. <sup>12,13</sup> A proton, with a size of ~0.89 fm (femtometer, 10<sup>-15</sup> m) in radius, <sup>14</sup> is five orders of magnitude smaller than the smallest metal ion—Li<sup>+</sup> (76 pm). <sup>15</sup> Thus, the "invisible" protons may be associated with negligible structural strain/stress for topotactic insertion reactions, which may facilitate long-term cycling stability. More importantly, the charges of protons can transport via structural diffusion, known as the Grotthuss mechanism <sup>16,17</sup> where the concerted breaking and reformation of the "H—O" covalent bonds of water and the "H···O" hydrogen bonds can deliver protons instantly wherever a hydrogen-bonded network goes. Therefore, a

proton battery would be of high rate capability if the Grotthuss mechanism is allowed to take place during redox reactions.

To date, a variety of anode materials have been demonstrated viable for proton storage in acidic electrolytes such as carbon materials; <sup>18</sup> organic crystals, for example, perylenetetracarboxylic dianhydride; pyrene-4,5,9,10-tetraone; <sup>9,19</sup> polymers; <sup>8</sup> metal oxides, for example, WO<sub>3</sub>· 0.6H<sub>2</sub>O<sup>13</sup> and MoO<sub>3</sub>; <sup>20</sup> and MXenes, for example, Ti<sub>3</sub>C<sub>2</sub>T<sub>x</sub>· <sup>21,22</sup> By contrast, less progress has been made on the cathode side. Wang et al. reported the consecutive coinsertion of H<sup>+</sup> and Zn<sup>2+</sup> in manganese dioxide in mild acidic electrolytes. <sup>23</sup> Most recently, our group presented a Turnbull's blue analogue (TBA) of Cu[Fe(CN)<sub>6</sub>]<sub>0.63</sub>·3.4H<sub>2</sub>O as a proton electrode, which revealed the power of Grotthuss topochemistry for high rate and exceptional cycling performance. <sup>12</sup> In fact, TBA pertains to a class of defective Prussian

Received: November 8, 2019 Accepted: February 3, 2020 Published: February 3, 2020



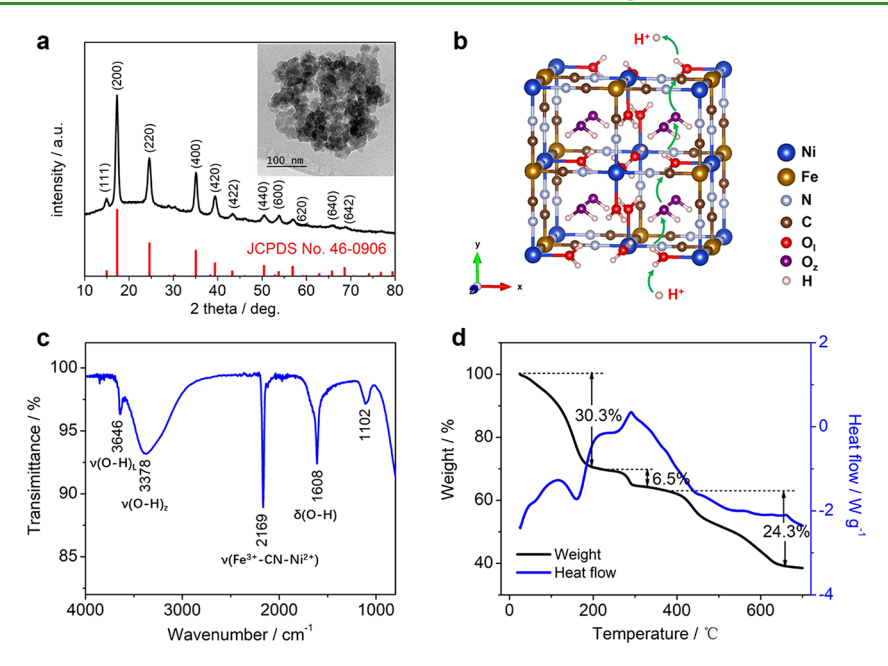


Figure 1. Characterization of the NiFe-TBA material. (a) XRD pattern. The inset is a TEM image. (b) Schematic of the crystal structure where  $O_L$  and  $O_z$  represent the oxygen atoms in ligand and zeolitic water molecules, respectively. The green arrows point to a tentative proton conduction pathway via the Grotthuss mechanism. (c) FTIR spectrum. (d) TGA-DSC curve under a  $N_2$  atmosphere.

blue analogs (PBA) with a theoretical stoichiometry of  $M^{II}[Fe^{III}(CN)_6]_{2/3}\cdot \Box_{1/3}\cdot 4H_2O$  ( $\Box$  represents the Fe(CN)<sub>6</sub> vacancies)<sup>24</sup> where the transition metal sites remain readily tunable with different metals such as Mn, Co, Ni, and Cu. However, the proton storage properties in these TBA structures have yet to be investigated systematically.

Here, we demonstrated Ni[Fe(CN)<sub>6</sub>]<sub>2/3</sub>·4H<sub>2</sub>O (NiFe-TBA) as an excellent proton-insertion cathode, which shows a reversible capacity of  $\sim$ 65 mAh g<sup>-1</sup>, the theoretical capacity, and stable cycling of 1000 cycles. It exhibits an ultrafast rate performance of 6000 C (390 A g<sup>-1</sup>) at room temperature. Particularly, NiFe-TBA retains a half of its theoretical capacity at a low temperature of -40 °C in an aqueous electrolyte. Our work further showcases the virtue of the Grotthuss mechanism in building high-rate proton batteries.

## ■ RESULTS AND DISCUSSION

In our previous work, we have learned that NiFe-TBA exhibits much better cycling performance than MnFe- and CoFe-TBAs, 12 which motivates us to study NiFe-TBA for proton storage. We prepared NiFe-TBA by a precipitation reaction with NiSO<sub>4</sub> and K<sub>3</sub>Fe(CN)<sub>6</sub> salts in an aqueous solution. Figure 1a shows its X-ray diffraction (XRD) pattern, which is indexed to the standard compound of Ni[Fe(CN)<sub>6</sub>]<sub>2/3</sub>·4H<sub>2</sub>O (JCPDS no. 46-0906). Figure 1b shows the schematic of its structure where the alternating connections of Fe-C and Ni-N bonds through the cyanide groups build up a threedimensional porous framework.<sup>25</sup> The nanocavities in the subcubes are occupied by zeolitic water molecules. Furthermore, in contrast to an intact PBA structure, there are vacancies of 1/3 of the Fe(CN)<sub>6</sub> sites that are randomly distributed throughout the TBA's structure where these defects expose the Ni sites that are coordinated by ligand water molecules.<sup>24</sup> The presence of zeolitic and ligand water molecules is corroborated by the vibration peaks at 3378 and 3646 cm<sup>-1</sup>, respectively, in the Fourier transform infrared spectrum (FTIR) of NiFe-TBA (Figure 1c). 26 Figure 1d shows

the thermogravimetric analysis (TGA) and differential scanning calorimetry (DSC) curves of NiFe-TBA, which encompasses three processes: a weight loss of 30.3% from room temperature to 200 °C (endothermic), a rapid weight loss of 6.5% from 250 to 300 °C (exothermic), and the progressive weight loss of 24.3% over a wide temperature range of 400–700 °C (endothermic). The first process is attributed to the elimination of lattice water molecules, which exceeds the reported water content of 10–25 wt % in conventional PBAs. The second step pertains to an exothermic reaction, which may correspond to the oxidization of cyanide groups by Fe<sup>3+</sup> ions and the resultant gas release. The last process is associated with multiple complicated reactions such as the entire framework decomposition thorough gas release and the formation of metal carbides. The second step per second step

The hydrogen-bonding network of lattice water molecules renders the Grotthuss mechanism viable inside the TBA structures. 27,32,33 In our recent work, we simulated the configuration of the hydrogen-bonding network in CuFe-TBA, which results in a low activation energy of 0.15 eV for proton conduction.<sup>12</sup> Of note, a low energy barrier of <0.4 eV suggests that the Grotthuss proton conduction takes place. 32,33 Considering the very similar structures of NiFe-TBA and CuFe-TBA, we postulate the proton conduction pathways via the hydrogen-bonding network of the ligand and zeolitic water molecules in NiFe-TBA (Figure 1b). The chemical formula of this compound is determined as Ni[Fe(CN)<sub>6</sub>]<sub>0.60</sub>· $\square$ <sub>0.40</sub>· 4.5H<sub>2</sub>O, on the basis of the inductively coupled plasma optical emission spectrometry (ICP-OES) on Ni and Fe elements, elemental analysis on C and N elements, and TGA on water (Table S1). The morphology of NiFe-TBA appears as irregular nanoparticles with a size distribution of 20-30 nm (Figure 1a inset), where the small particle sizes primarily result from the instant crystallization process during rapid precipitation.

We evaluated the proton (de)insertion performance of NiFe-TBA in 1.0 mol  $L^{-1}$   $H_2SO_4$  as the electrolyte in three-electrode cells. Figure 2a shows the galvanostatic charge/

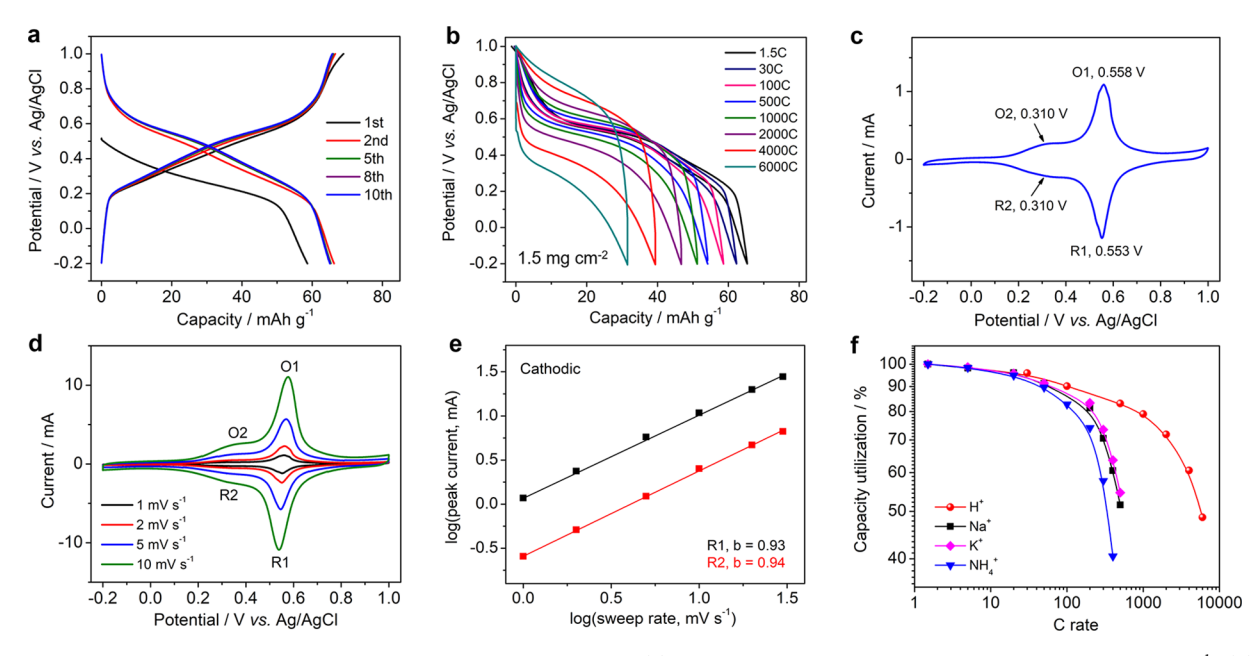


Figure 2. Electrochemical characterization of the NiFe-TBA electrode. (a) GCD potential profiles at a current rate of 100 mA  $g^{-1}$ . (b) Rate performance. Here, 1 C is defined as 65 mA  $g^{-1}$ . (c) CV curves of H<sup>+</sup> (de)insertion at 1 mV  $s^{-1}$ . (d) CV curves at different scan rates. (e) Correlation between the cathodic current and scan rate. (f) Rate comparison for H<sup>+</sup>, Na<sup>+</sup>, K<sup>+</sup>, and NH<sub>4</sub><sup>+</sup> insertion.

discharge (GCD) potential profiles at 100 mA  $g^{-1}$  where after the initial activation process, NiFe-TBA delivers a reversible capacity of ~65 mAh  $g^{-1}$ , corresponding to the full utilization of the theoretical capacity. Importantly, the polarization between the charge and discharge is only 37 mV for H<sup>+</sup> (de)insertion (Figure S1a), which is comparable to Na<sup>+</sup> but much smaller than K<sup>+</sup> and NH<sub>4</sub><sup>+</sup> (de)insertion at the same current rate (Figure S1b-d). Generally, a small extent of polarization implies fast insertion kinetics and, sometimes, is characteristic of the pseudocapacitive insertion.<sup>34</sup>

Of note, the NiFe-TBA electrode shows an outstanding rate performance (Figure 2b), where the discharge capacity is  $\sim$ 65, 62, 59, 54, 51, 47, and 39 mAh  $g^{-1}$  at the current rates of 1.5, 30, 100, 500, 1000, 2000, and 4000 C, respectively. Even at an extremely high rate of 6000 C (390 A g-1), NiFe-TBA still retains a discharge capacity of ~31 mAh g<sup>-1</sup>, which is approximately 50% of the theoretical capacity. Coincidently, the CuFe-TBA electrode also shows capacity utilization of ~50% at a comparable rate of 4000 C ( $\overline{380}$  A  $g^{-1}$ ). Such a record high rate behavior of NiFe-TBA corresponds to an extremely brief charge or discharge time of ~0.28 seconds and outperforms most of the best insertion or capacitive electrodes. 21,34,35 Table S2 compares the performance of NiFe-TBA with the reported high-rate electrodes. Additionally, we found that the polarization between charge and discharge increases linearly with the current rate (Figure S2). According to Ohm's law, the voltage is the product of current and electrical resistance when the current passes through a conductor.<sup>36</sup> Thus, the potential hysteresis of the NiFe-TBA electrodes is predominantly contributed by the electrical resistance of testing cells.3

To better understand the proton insertion process, we collected cyclic voltammetry (CV) curves at different scan rates (Figure 2c,d). When tested at a low scan rate of 1 mV s<sup>-1</sup> (Figure 2c), there are two pairs of symmetrical oxidization/reduction peaks at 0.558/0.553 V (O1/R1) and 0.310/0.310 V (O2/R2), respectively, where their low potential gaps of 5 and 0 mV reveals the kinetic reversibility, that is, a pseudocapa-

citive behavior.<sup>38</sup> Note that the current i and the scan rate  $\nu$  can be correlated by the equation of  $i = av^b$ , where b is 0.5 or 1 depending on if the reaction is diffusion-controlled or capacitive.<sup>38</sup> When tested at the scan rate of 1–30 mV s<sup>-1</sup>, the respective b values for the cathodic peaks R1 and R2 are 0.93 and 0.94 (Figure 2e), close to unity, which further substantiates the capacitive proton (de)insertion. The b values of the anodic peaks O1 and O2 are calculated as 0.96 and 1.01, respectively (Figure S3). The CV curves measured at higher scan rates of 50–1000 mV s<sup>-1</sup> are provided in Figure S4.

The fast proton insertion likely results from the Grotthuss proton conduction, which could efficiently and rapidly transport protons. By contrast, the metal ions of Na<sup>+</sup> and K<sup>+</sup>, as well as the non-metal ions of NH<sub>4</sub><sup>+</sup>, cannot activate the Grotthuss mechanism, which incurs smaller lower b values of 0.75, 0.71, and 0.81, respectively (Figures S5-S7). This also accounts for their comparatively inferior rate performance where these ions can only afford a much lower rate capability of 300-500 C (Figure 2f and Figure S8). The observation here also agrees well with our previous results on the CuFe-TBA electrode. 12 We note that NiFe-TBA exhibits two pairs of redox peaks for H<sup>+</sup> (de)insertion (Figure 2c), which differs from the single pair for Na<sup>+</sup>, K<sup>+</sup>, and NH<sub>4</sub><sup>+</sup> (de)insertion. One plausible explanation could be the binding of protons with two types of water molecules, that is, ligand and zeolitic, in the TBA structure. To further understand the proton (de)insertion, we carried out electrochemical quartz crystal microbalance (EQCM) analysis on the NiFe-TBA electrode (Figure S9) where the O2 and O1 peaks are associated with mass decrease (water expulsion) and mass increase (water incorporation), respectively. The distinct water migration processes may give rise to different binding energies of protons, which are likely responsible for the two pairs of redox peaks.<sup>13</sup>

Besides the superior  $H^+$  insertion rate, the NiFe-TBA electrode also exhibits a relatively stable cycling performance where the capacity retention is  $\sim$ 73% over 1000 cycles at a 10 C rate (Figure S10). When cycled at a lower rate of 2 C, NiFe-

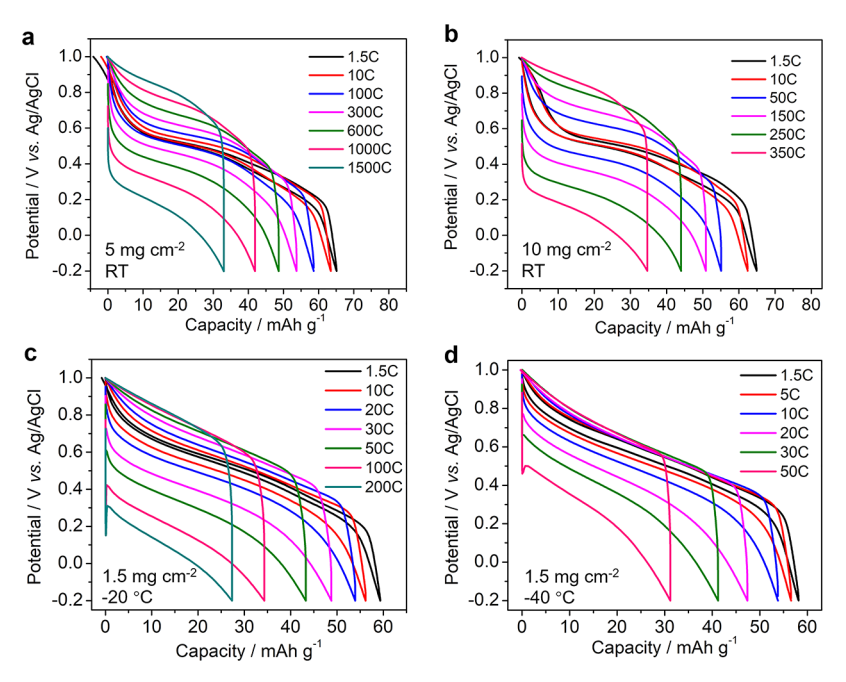


Figure 3. Rate performance of the NiFe-TBA electrode. (a) Rate performance at the active mass loading of 5 mg cm<sup>-2</sup> at room temperature. (b) Rate performance at 10 mg cm<sup>-2</sup> at room temperature. (c) Rate performance at 1.5 mg cm<sup>-2</sup> at -20 °C. (d) Rate performance at  $\sim$ 1.5 mg cm<sup>-2</sup> at -40 °C.

Table 1. Low-Temperature Performance of some Representative Electrodes

electrodes	electrolytes	temperature (°C)	capacity utilization at low temperature	rate performance
$\text{Li}_{3}\text{V}_{2}(\text{PO}_{4})_{3} + \\ \text{Li}\text{Ti}_{2}(\text{PO}_{4})_{3}^{41}$	21 M LiTFSI, aqueous	-20	0.2 C, 80% utilization of room temperature (RT)	6 C, 800 mA g <sup>-1</sup> , 64% utilization
LiFePO <sub>4</sub> <sup>42</sup>	1.0 M aqueous Li <sub>2</sub> SO <sub>4</sub> + 40% ethylene glycol	-20	0.2 C, 61% utilization of RT	1 C, 130 mA g <sup>-1</sup> , 50% utilization
PAQS <sup>19</sup>	10 M KOH, aqueous	-25	0.5 C, 90% utilization of RT	10 C, 2000 mA g <sup>-1</sup> , 86% utilization
LiCoO <sub>2</sub> <sup>43</sup>	saturated LiCl, aqueous	-40	0.2 C rate, 77% utilization of RT	0.5 C, 45 mA $g^{-1}$ , 57% utilization
NiFe-TBA this work	1.0 M H <sub>2</sub> SO <sub>4</sub> , aqueous	-40,	1.5 C, 89% utilization of RT	50 C, 3250 mA g <sup>-1</sup> , 50% utilization
$NaTi_2(PO_4)_3^{44}$	2.0 M NaClO <sub>4</sub> + DMSO, hybrid	-50	0.5 C, 60% utilization of RT	10 C, 1330 mA g <sup>-1</sup> , 77% utilization
$Na_2FeFe(CN)_6^{40}$	1.0 M NaClO <sub>4</sub> in EC/PC, nonaqueous	-25	0.1 C, 85% utilization of RT	6 C, 900 mA $g^{-1}$ , ~50% utilization
PTPAn and PNTCDA <sup>45</sup>	2.0 M LiTFSI in ethyl acetate, nonaqueous	-40	0.5 C, ~100% utilization of RT	5 C, 500 mA g <sup>-1</sup> , 64% utilization
		-70	0.5 C, ~70% utilization of RT	5 C, 500 mA $g^{-1}$ , 20% utilization
LiCoO <sub>2</sub> <sup>46</sup>	0.2 M LiTFSI in fluoromethane and $CO_2$	-60	0.1 C, ~60.6% utilization of RT	0.2 C, 27 mA $g^{-1}$ , 0% utilization
CNT capacitors <sup>47</sup>	eutectic ionic liquids mixture, nonaqueous	-50	100 mV s $^{-1}$ , $\sim$ 100% utilization of RT	5 mV s <sup>-1</sup> , $\sim$ 100% utilization

"The abbreviations of LiTFSI, PAQS, PTPAn, PNTCDA, and CNT represent lithium bis(trifluoromethanesulfonyl)imide, poly(anthraquinonyl sulfide), polytriphenylamine, polyimide 1,4,5,8-naphthalenetetracarboxylic dianhydride, and carbon nanotube, respectively.

TBA retains  $\sim$ 78% of its initial capacity after 150 cycles (Figure S11). In comparison with CuFe-TBA, the inferior cycling stability of NiFe-TBA likely results from the dissolution of Ni<sup>2+</sup> ions in the acidic electrolytes (Figure S11).

Remarkably, the high rate performance of NiFe-TBA is also amenable to both high mass loadings and low-temperature conditions. When the active mass loading is increased to 5 mg cm<sup>-2</sup>, the NiFe-TBA electrode retains ~50% of its theoretical capacity at 1500 C (Figure 3a). Even at a high mass loading of 10 mg cm<sup>-2</sup>, it delivers more than a half of its theoretical capacity at 350 C (Figure 3b). Note that the high mass loading

gives rise to a respectable areal capacity of  $\sim 0.65$  Ah cm<sup>-2</sup>. To gain understanding on the reaction kinetics at higher mass loadings, we collected CV curves of NiFe-TBA electrodes at 5 and 10 mg cm<sup>-2</sup> at varying scan rates. At 5 mg cm<sup>-2</sup>, the b value is still as high as 0.96 (Figure S12), which indicates the pseudocapacitive proton storage behavior; the b value decreases to 0.80 at 10 mg cm<sup>-2</sup> (Figure S13). The lowered b values at 10 mg cm<sup>-2</sup> somehow indicates that the b values are limited in revealing the fundamental ion-charge-storage mechanisms, and the engineering-related factors also affect the b values, such as the thickness of electrodes.

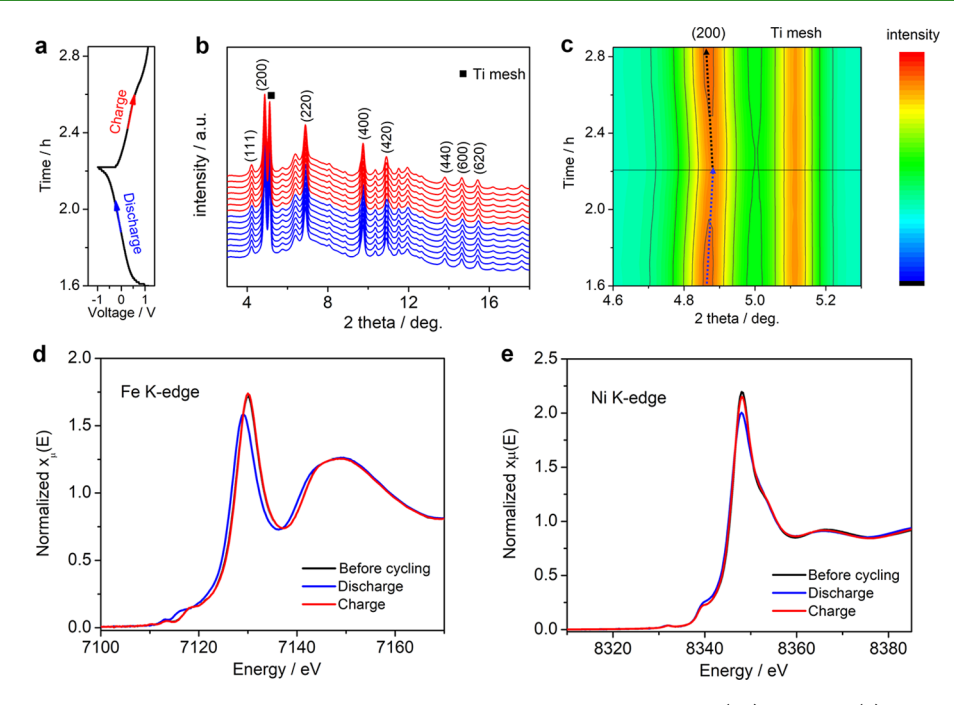


Figure 4. Structural evolution and valence state change of the NiFe-TBA electrode during proton (de)insertion. (a) Typical GCD profiles at 2 C. (b) In operando Synchrotron XRD patterns. (c) Contour plot of the (200) peak. (d) Fe K-edge XANES results. (e) Ni K-edge XANES results.

The fast proton insertion also facilitates the low-temperature performance. Figure S14 shows the comparison of the GCD curves of NiFe-TBA at room temperature, -20 °C, and -40 °C, which deliver a comparable capacity of 65, 60, and 58 mAh g<sup>-1</sup>, respectively. The seemingly "higher" insertion potential is likely due to the potential shift of the Ag/AgCl reference electrode, whose potential decreases at a lower temperature.<sup>35</sup> Figure 3c shows the rate performance of NiFe-TBA at -20 °C, which realizes a ~45% capacity utilization at a 200 C rate. Even at -40 °C, it affords a high rate capability of 50 C with  $\sim 50\%$ of theoretical capacity (Figure 3d, Figure S15). We also tested the rate performance of NiFe-TBA at both ~10 mg cm<sup>-2</sup> and -40 °C, which still retains a ~60% capacity utilization at an 8 C rate (Figure S16). Electrochemical impedance spectra (EIS) reveal that from room temperature to -40 °C, the charge transfer resistance of NiFe-TBA cells has increased from ~0.8 to ~170 ohms (Figure S16), whereas the ionic conductivity of H<sub>2</sub>SO<sub>4</sub> electrolytes has decreased from 260 to 6 mS cm<sup>-1</sup> (Figure S17). Thus, we deem that at such a high mass loading and a low temperature, the charge transfer is the ratecontrolling step for proton (de)insertion. Goodenough et al. also reported similar phenomenon on Na<sub>2</sub>FeFe(CN)<sub>6</sub> compounds for Na<sup>+</sup> storage at a low temperature.<sup>40</sup>

To our knowledge, such outstanding performance at a low temperature has been rarely reported for aqueous batteries, which is competitive to some nonaqueous batteries. To have a picture of the context, Table 1 lists the capacity utilization and rate performance of some representative low-temperature electrode/electrolyte systems where NiFe-TBA stands out due to its high capacity utilization of 89% at  $-40\,^{\circ}\mathrm{C}$  and also the impressive rate of 50 C (3250 mA g $^{-1}$ ) at such a low temperature.

In the liquid water state, water molecules can constantly break and reform hydrogen bonds and thus migrate freely in the bulk liquid phase, while in the solid ice state, water molecules lose their kinetic energy and get trapped at crystal positions in ice.<sup>48</sup> Interestingly, based on the H<sub>2</sub>SO<sub>4</sub>/H<sub>2</sub>O

phase diagram,  $^{49,50}$  the 1.0 mol  $L^{-1}\;H_2SO_4$  electrolyte will not be completely frozen until -76 °C, which comprises the liquid sulfuric acid hydrate, crystalline ice, and some liquid phase at -40 °C (Figure S18). We postulate that it is the H<sub>2</sub>SO<sub>4</sub> solution that serves as the primary proton conduit; however, it begs the question of whether proton can be conducted through the ice. Most recently, an ice-salt composite has been reported to serve as a viable solid-state electrolyte for various ion insertion systems.<sup>51</sup> We envision that the proton storage at subzero temperature would be an attractive avenue for energy storage. An interesting question is whether the lattice water molecules are frozen in the TBA's structure at -40 °C. Different from the bulk water, the chemical environment of lattice water molecules confined in NiFe-TBA's lattice is very different. Indeed, at −40 °C, the rate performance of TBA is lower than that at room temperature. Yet, note that the conductivity of the electrolyte of H2SO4 dramatically decreases as this electrolyte is largely frozen at -40 °C, which should contribute a great deal to the decreased rate capability of the TBA testing cells. However, the fact that at -40 °C where the TBA electrode still exhibits more than a half of optimal capacity at 50 C says that the Grotthuss mechanism is still applicable for the hydrogen-bonding network of lattice water molecules in the TBA's structure at that temperature. The operation of the Grotthuss mechanism requires that water molecules vibrate and adjust their spatial locations in the lattice of TBA. Thus, at -40 °C, lattice water molecules in the TBA lattice can still vibrate and rotate, albeit in a more sluggish

To investigate the proton insertion process, we performed in operando synchrotron XRD to analyze the structural evolution during charge—discharge processes. Figure 4a shows the GCD curves of the testing cells at a 2 C rate, which comprises NiFe-TBA as the working electrode and activated carbon as the counter electrode. Figure 4b displays the overall XRD patterns where there is no significant change in the XRD patterns, indicating that NiFe-TBA maintains the cubic structure during

the entire proton (de)insertion processes. The solid-solution reaction also explains the S-shaped GCD profiles (Figure 2a). To further inspect the lattice evolution, Figure 4c shows the contour plot of the (200) peak where during discharge, it shifts rightward from 4.868 to 4.880°, which corresponds to the lattice shrinkage from 10.22 to 10.19 Å. This can be attributed to the smaller radius of  $[Fe^{II}(CN)_6]^{4-}$  than  $[Fe^{III}(CN)_6]^{3-}$  anions. <sup>52,53</sup> During charge, the (200) peak progressively restores to its original position, which corresponds to a reversible lattice evolution. The overall volume change is thus determined as low as 0.88%, lower than 1%, which pertains to a zero-strain insertion material. Recently, Guo et al. reported that a potassium nickel hexacyanoferrate of  $K_{0.09}Ni[Fe(CN)_6]_{0.71} \cdot 6H_2O$  also experienced a zero-strain  $Na^+$  insertion process.

The reversible capacity of 65 mAh g<sup>-1</sup> corresponds to a oneelectron transfer reaction. To clarify whether the Fe or Ni ions serve as the redox center, we carried out in situ X-ray absorption near-edge spectra (XANES) analysis on the NiFe-TBA electrode. As shown in Figure 4d,e, during discharge, the Fe K-edge shifts from 7130.0 to 7128.9 eV, indicative of the Fe<sup>3+</sup>/Fe<sup>2+</sup> reduction, while there is no appreciable change for the Ni K-edge spectra. While during charge, the Fe K-edge recovers to its initial position, and the Ni K-edge still maintains in the same position. Thus, we can conclude that it is the Fe ions that participate in the redox reaction, whereas the inert Ni sites may stabilize the structure for repeated GCD cycles.

# CONCLUSIONS

In summary, we presented a hydrous nickel—iron Turnbull's blue as a promising proton electrode, which exhibits an extremely high rate capability of 6000 C. The fast proton insertion kinetics also render a high rate performance of 350 C at the mass loading of  $\sim\!10$  mg cm $^{-2}$  and a 50 C rate at the super-low temperature of -40 °C. Our work further demonstrates the power of the Grotthuss mechanism in building high-rate proton batteries, which may shed some light on the energy storage under extreme conditions.

## **■ EXPERIMENTAL SECTION**

**Material Synthesis.** The synthesis of NiFe-TBA was based on a precipitation reaction in an aqueous solution. In a typical procedure, the NiSO<sub>4</sub> solution (40 mL 0.16 mol L<sup>-1</sup>) was added dropwise into the  $\rm K_3Fe(CN)_6$  solution (40 mL 0.1 mol L<sup>-1</sup>) under stirring. After 6 hrs of reaction, the yellow precipitates were washed and centrifuged with deionized water and ethanol for multiple times and then allowed to dry in a petri dish naturally at room temperature.

Material Characterization. The XRD patterns were collected on a Rigaku Ultima IV Diffractometer (Cu K $\alpha$  irradiation,  $\lambda = 1.5406$  Å). The FTIR spectra were recorded on a NICOLET 5397 AVATAR 360 FTIR spectrometer. The water amount in NiFe-TBA was analyzed by thermogravimetric analysis (TGA, SDTQ600), and the analysis of carbon and nitrogen content was conducted by the elemental analysis (Elementar Vario Macro Cube). The content of the nickel and iron elements was analyzed by inductively coupled plasma optical emission spectrometry (ICP-OES, Perkin Elmer 2100 DV). Transmission electron microscopy images of the NiFe-TBA material were observed on a JEOL-2010 microscope. The in operando synchrotron X-ray diffraction was carried out at the experimental station 13-BM-C of the Advanced Photon Source, Argonne National Laboratory. The X-ray beam has been monochromated by the silicon 311 crystal as 28.6 keV (0.434 Å). We collected the diffraction patterns in a transmission way, and we placed the MAR165 Charge Coupled Device (CCD) detector (Rayonix) ~1.80 cm away from the sample. Each diffraction pattern has been typically exposed for 60 s. The distance has been calibrated

by the Ti mesh current collector inside the 2032-type coin cells. The synchrotron X-ray diffraction patterns were further analyzed by the DIOPTAS software (Prescher and Prakapenka, 2015). The in situ XANES measurements of the Fe and Ni K-edges of NiFe-TBA electrodes were tested at the Advanced Photon Source (APS), which utilizes the 9-BM-B bending-magnet beamline with an electron energy of 7 GeV plus an average current of 100 mA. The radiation has been monochromatized by the silicon (111) double-crystal monochromator. All the XANES spectra were recorded in a transmission mode. We calibrated the peak position of the 1st derivative of the Fe foil as 7112 eV. The analysis and reduction of the XANES data were conducted by the Athena software.

Electrochemical Tests. The working electrode consists of 70 wt % active mass of NiFe-TBA, 20 wt % Ketjen Black carbon, and 10 wt % polyvinylidene fluoride (PVdF) binder. The slurry was cast on the carbon fiber paper (Fuel Cells Etc), with an active mass loading of  $\sim$ 1.5 mg cm<sup>-2</sup>. We also prepared the thick electrodes with active mass loadings of  $\sim$ 5.0 and  $\sim$ 10.0 mg cm<sup>-2</sup>, which are composed of  $\sim$ 58.3 wt % NiFe-TBA, ~16.7 wt % KB, and ~25 wt % PVdF. The electrochemical performance was evaluated in three-electrode Swagelok cells, which comprise the NiFe-TBA as the working electrode, a large piece of activated carbon self-standing film as the counter electrode, and Ag/AgCl as the reference electrode (E =+0.197 V vs standard hydrogen electrode). The electrolytes for H<sup>+</sup>  $Na^+$ ,  $K^+$ , and  $NH_4^+$  insertion are 1.0 mol  $L^{-1}$   $H_2SO_4$ , 1.0 mol  $L^{-1}$  $Na_2SO_4$ , 0.8 mol L<sup>-1</sup>  $K_2SO_4$ , and 1.0 mol L<sup>-1</sup>  $(NH_4)_2SO_4$ , respectively. The separators are 2-3 layers of regular Whatman filter papers. The low-temperature performance of NiFe-TBA was examined in the Thermotron S-1.2C temperature chamber. The ionic conductivity of H2SO4 electrolytes was tested by electrochemical impedance spectra (EIS), which are ~260 and ~6 mS cm<sup>-1</sup> at room temperature and -40 °C, respectively. The cyclic voltammetry (CV), galvanostatic charge/discharge (GCD), and rate performance tests were conducted on a VMP-3 multi-channel workstation. The cycling performance was tested on the Landt battery cycler (CT2001A). The EIS results of NiFe-TBA electrodes were tested on the VMP-3 multichannel workstation with an oscillation amplitude of 10 mV and frequency from 1 MHz to 0.1 Hz. The electrochemical quartz crystal microbalance (EQCM) tests were conducted on a QCM200 quartz crystal microbalance.

## ASSOCIATED CONTENT

## Supporting Information

The Supporting Information is available free of charge at https://pubs.acs.org/doi/10.1021/acsami.9b20320.

Experimental details on the material/electrode preparation and electrochemical performance (CV, GCD, rate, and cycling) (PDF)

## AUTHOR INFORMATION

#### **Corresponding Authors**

Jun Lu − Chemical Sciences and Engineering Division, Argonne National Laboratory, Lemont, Illinois 60439, United States; orcid.org/0000-0003-0858-8577; Email: junlu@anl.gov Xiulei Ji − Department of Chemistry, Oregon State University, Corvallis, Oregon 97331, United States; orcid.org/0000-0002-4649-9594; Email: david.ji@oregonstate.edu

#### **Authors**

Xianyong Wu — Department of Chemistry, Oregon State University, Corvallis, Oregon 97331, United States Shen Qiu — Department of Chemistry, Oregon State University, Corvallis, Oregon 97331, United States Yunkai Xu — Department of Chemistry, Oregon State University, Corvallis, Oregon 97331, United States

- Lu Ma X-ray Science Division, Advanced Photon Sources, Argonne National Laboratory, Lemont, Illinois 60439, United States
- **Xuanxuan Bi** Chemical Sciences and Engineering Division, Argonne National Laboratory, Lemont, Illinois 60439, United States
- Yifei Yuan Chemical Sciences and Engineering Division, Argonne National Laboratory, Lemont, Illinois 60439, United States; Department of Mechanical and Industrial Engineering, University of Illinois at Chicago, Chicago, Illinois 60607, United States
- **Tianpin Wu** X-ray Science Division, Advanced Photon Sources, Argonne National Laboratory, Lemont, Illinois 60439, United States
- Reza Shahbazian-Yassar Department of Mechanical and Industrial Engineering, University of Illinois at Chicago, Chicago, Illinois 60607, United States; orcid.org/0000-0002-7744-4780

Complete contact information is available at: https://pubs.acs.org/10.1021/acsami.9b20320

### **Author Contributions**

The manuscript was written through contributions of all authors. All authors have given approval to the final version of the manuscript.

#### **Funding**

X.J. acknowledges the financial support from the US National Science Foundation (award number 1551693). Work at Argonne National Laboratory was supported by the US Department of Energy (DOE), Office of Energy Efficiency and Renewable Energy, Vehicle Technologies Office. Argonne National Laboratory is operated for DOE Office of Science by UChicago Argonne, LLC, under contract number DE-AC02-06CH11357. This research used resources of the APS (9-BM and 11-ID-D), a US DOE Office of Science User Facility operated for the DOE Office of Science by Argonne National Laboratory under contract DE-AC02-06CH11357. R.S.-Y. acknowledges the financial support from NSF DMR-1809439. This work made use of instruments in the Electron Microscopy Service (Research Resources Center, UIC).

#### **Notes**

The authors declare no competing financial interest.

#### REFERENCES

- (1) Zhu, L.; Ding, G.; Xie, L.; Cao, X.; Liu, J.; Lei, X.; Ma, J. Conjugated Carbonyl Compounds as High-Performance Cathode Materials for Rechargeable Batteries. *Chem. Mater.* **2019**, *31*, 8582–8612.
- (2) Yuan, Y.; Lu, J. Demanding Energy from Carbon. *Carbon Energy* **2019**, *1*, 8–12.
- (3) Qiu, S.; Wu, X.; Wang, M.; Lucero, M.; Wang, Y.; Wang, J.; Yang, Z.; Xu, W.; Wang, Q.; Gu, M.; Wen, J.; Huang, Y.; Xu, Z. J.; Feng, Z. Nasicon-Type Na<sub>3</sub>Fe<sub>2</sub>(PO<sub>4</sub>)<sub>3</sub> as a Low-Cost and High-Rate Anode Material for Aqueous Sodium-Ion Batteries. *Nano Energy* 2019, 64, 103941
- (4) Lin, X.; Sun, Q.; Doyle Davis, K.; Li, R.; Sun, X. The Application of Carbon Materials in Nonaqueous Na-O<sub>2</sub> Batteries. *Carbon Energy* **2019**, *1*, 141–164.
- (5) Ding, X.; Zhang, F.; Ji, B.; Liu, Y.; Li, J.; Lee, C.-S.; Tang, Y. Potassium Dual-Ion Hybrid Batteries with Ultrahigh Rate Performance and Excellent Cycling Stability. *ACS Appl. Mater. Interfaces* **2018**, *10*, 42294–42300.
- (6) Bin, D.; Liu, Y.; Yang, B.; Huang, J.; Dong, X.; Zhang, X.; Wang, Y.; Xia, Y. Engineering a High-Energy-Density and Long Lifespan

- Aqueous Zinc Battery Via Ammonium Vanadium Bronze. ACS Appl. Mater. Interfaces 2019, 11, 20796—20803.
- (7) Wan, F.; Zhang, Y.; Zhang, L.; Liu, D.; Wang, C.; Song, L.; Niu, Z.; Chen, J. Reversible Oxygen Redox Chemistry in Aqueous Zinc-Ion Batteries. *Angew. Chem. Int. Ed.* **2019**, *58*, 7062–7067.
- (8) Emanuelsson, R.; Sterby, M.; Strømme, M.; Sjödin, M. An All-Organic Proton Battery. J. Am. Chem. Soc. 2017, 139, 4828–4834.
- (9) Wang, X.; Bommier, C.; Jian, Z.; Li, Z.; Chandrabose, R. S.; Rodríguez-Pérez, I. A.; Greaney, P. A.; Ji, X. Hydronium-Ion Batteries with Perylenetetracarboxylic Dianhydride Crystals as an Electrode. *Angew. Chem.* **2017**, *129*, 2955–2959.
- (10) Wessells, C. D.; Peddada, S. V.; McDowell, M. T.; Huggins, R. A.; Cui, Y. The Effect of Insertion Species on Nanostructured Open Framework Hexacyanoferrate Battery Electrodes. *J. Electrochem. Soc.* **2011**, *159*, A98–A103.
- (11) Wu, X.; Xu, Y.; Jiang, H.; Wei, Z.; Hong, J. J.; Hernandez, A. S.; Du, F.; Ji, X. NH<sub>4</sub><sup>+</sup> Topotactic Insertion in Berlin Green: An Exceptionally Long-Cycling Cathode in Aqueous Ammonium-Ion Batteries. *ACS Appl. Energy Mater.* **2018**, *1*, 3077–3083.
- (12) Wu, X.; Hong, J. J.; Shin, W.; Ma, L.; Liu, T.; Bi, X.; Yuan, Y.; Qi, Y.; Surta, T. W.; Huang, W.; Neuefeind, J.; Wu, T.; Greaney, P. A.; Lu, J.; Ji, X. Diffusion-Free Grotthuss Topochemistry for High-Rate and Long-Life Proton Batteries. *Nat. Energy* **2019**, *4*, 123.
- (13) Jiang, H.; Hong, J. J.; Wu, X.; Surta, T. W.; Qi, Y.; Dong, S.; Li, Z.; Leonard, D. P.; Holoubek, J. J.; Wong, J. C.; Razink, J. J.; Zhang, X.; Ji, X. Insights on the Proton Insertion Mechanism in the Electrode of Hexagonal Tungsten Oxide Hydrate. *J. Am. Chem. Soc.* **2018**, *140*, 11556–11559.
- (14) Carlson, C. E. The Proton Radius Puzzle. *Prog. Part. Nucl. Phys.* **2015**, 82, 59–77.
- (15) Wu, J.; Cao, Y.; Zhao, H.; Mao, J.; Guo, Z. The Critical Role of Carbon in Marrying Silicon and Graphite Anodes for High-Energy Lithium-Ion Batteries. *Carbon Energy* **2019**, *1*, 57–76.
- (16) Agmon, N. The Grotthuss Mechanism. Chem. Phys. Lett. 1995, 244, 456-462.
- (17) Gileadi, E.; Kirowa-Eisner, E. Electrolytic Conductivity—the Hopping Mechanism of the Proton and Beyond. *Electrochim. Acta* **2006**, *51*, 6003–6011.
- (18) Qu, D. Mechanism for Electrochemical Hydrogen Insertion in Carbonaceous Materials. *J. Power Sources* **2008**, *179*, 310–316.
- (19) Liang, Y.; Jing, Y.; Gheytani, S.; Lee, K.-Y.; Liu, P.; Facchetti, A.; Yao, Y. Universal Quinone Electrodes for Long Cycle Life Aqueous Rechargeable Batteries. *Nat. Mater.* **2017**, *16*, 841.
- (20) Wang, X.; Xie, Y.; Tang, K.; Wang, C.; Yan, C. Redox Chemistry of Molybdenum Trioxide for Ultrafast Hydrogen-Ion Storage. *Angew. Chem. Int. Ed.* **2018**, *57*, 11569–11573.
- (21) Lukatskaya, M. R.; Kota, S.; Lin, Z.; Zhao, M.-Q.; Shpigel, N.; Levi, M. D.; Halim, J.; Taberna, P.-L.; Barsoum, M. W.; Simon, P.; Gogotsi, Y. Ultra-High-Rate Pseudocapacitive Energy Storage in Two-Dimensional Transition Metal Carbides. *Nat. Energy* **2017**, *2*, 17105.
- (22) Wang, S.; Zhao, X.; Yan, X.; Xiao, Z.; Liu, C.; Zhang, Y.; Yang, X. Regulating Fast Anionic Redox for High-Voltage Aqueous Hydrogen-Ion-Based Energy Storage. *Angew. Chem.* **2019**, *131*, 211–216.
- (23) Sun, W.; Wang, F.; Hou, S.; Yang, C.; Fan, X.; Ma, Z.; Gao, T.; Han, F.; Hu, R.; Zhu, M.; Wang, C. Zn/MnO<sub>2</sub> Battery Chemistry with H<sup>+</sup> and Zn<sup>2+</sup>Coinsertion. *J. Am. Chem. Soc.* **2017**, *139*, 9775–9778.
- (24) Kaye, S. S.; Long, J. R. Hydrogen Storage in the Dehydrated Prussian Blue Analogues  $M_3[Co(CN)_6]_2$  (M= Mn, Fe, Co, Ni, Cu, Zn). J. Am. Chem. Soc. **2005**, 127, 6506–6507.
- (25) Wu, X.; Shao, M.; Wu, C.; Qian, J.; Cao, Y.; Ai, X.; Yang, H. Low Defect FeFe(CN)<sub>6</sub> Framework as Stable Host Material for High Performance Li-Ion Batteries. ACS Appl. Mater. Interfaces **2016**, 8, 23706–23712.
- (26) Avila, M.; Reguera, L.; Rodríguez-Hernández, J.; Balmaseda, J.; Reguera, E. Porous Framework of T<sub>2</sub>[Fe(CN)<sub>6</sub>]·xH<sub>2</sub>O with T= Co, Ni, Cu, Zn, and H<sub>2</sub> Storage. *J. Solid State Chem.* **2008**, *181*, 2899–2907.

- (27) Lee, J. H.; Ali, G.; Kim, D. H.; Chung, K. Y. Metal-Organic Framework Cathodes Based on a Vanadium Hexacyanoferrate Prussian Blue Analogue for High-Performance Aqueous Rechargeable Batteries. *Adv. Energy Mater.* **2017**, *7*, 1601491.
- (28) Pasta, M.; Wessells, C. D.; Liu, N.; Nelson, J.; McDowell, M. T.; Huggins, R. A.; Toney, M. F.; Cui, Y. Full Open-Framework Batteries for Stationary Energy Storage. *Nat. Commun.* **2014**, *5*, 3007.
- (29) Åkerblom, I. E.; Ojwang, D. O.; Grins, J.; Svensson, G. A Thermogravimetric Study of Thermal Dehydration of Copper Hexacyanoferrate by Means of Model-Free Kinetic Analysis. *J. Therm. Anal. Calorim.* **2017**, *129*, 721–731.
- (30) You, Y.; Wu, X.-L.; Yin, Y.-X.; Guo, Y.-G. A Zero-Strain Insertion Cathode Material of Nickel Ferricyanide for Sodium-Ion Batteries. *J. Mater. Chem. A* **2013**, *1*, 14061–14065.
- (31) Aparicio, C.; Machala, L.; Marusak, Z. Thermal Decomposition of Prussian Blue under Inert Atmosphere. *J. Therm. Anal. Calorim.* **2012**, *110*, 661–669.
- (32) Ono, K.; Ishizaki, M.; Kanaizuka, K.; Togashi, T.; Yamada, T.; Kitagawa, H.; Kurihara, M. Grain-Boundary-Free Super-Proton Conduction of a Solution-Processed Prussian-Blue Nanoparticle Film. *Angew. Chem. Int. Ed.* **2017**, *56*, 5531–5535.
- (33) Ohkoshi, S.-i.; Nakagawa, K.; Tomono, K.; Imoto, K.; Tsunobuchi, Y.; Tokoro, H. High Proton Conductivity in Prussian Blue Analogues and the Interference Effect by Magnetic Ordering. *J. Am. Chem. Soc.* **2010**, *132*, 6620–6621.
- (34) Augustyn, V.; Come, J.; Lowe, M. A.; Kim, J. W.; Taberna, P.-L.; Tolbert, S. H.; Abruña, H. D.; Simon, P.; Dunn, B. High-Rate Electrochemical Energy Storage through Li<sup>+</sup> Intercalation Pseudocapacitance. *Nat. Mater.* **2013**, *12*, 518–522.
- (35) Zhang, H.; Yu, X.; Braun, P. V. Three-Dimensional Bicontinuous Ultrafast-Charge and -Discharge Bulk Battery Electrodes. *Nat. Nanotechnol.* **2011**, *6*, 277.
- (36) Nyman, A.; Zavalis, T. G.; Elger, R.; Behm, M.; Lindbergh, G. Analysis of the Polarization in a Li-Ion Battery Cell by Numerical Simulations. *J. Electrochem. Soc.* **2010**, *157*, A1236—A1246.
- (37) Wessells, C. D.; Huggins, R. A.; Cui, Y. Copper Hexacyanoferrate Battery Electrodes with Long Cycle Life and High Power. *Nat. Commun.* **2011**, *2*, 550.
- (38) Wang, J.; Polleux, J.; Lim, J.; Dunn, B. Pseudocapacitive Contributions to Electrochemical Energy Storage in TiO<sub>2</sub> (Anatase) Nanoparticles. *J. Phys. Chem. C* **2007**, *111*, 14925–14931.
- (39) Sawyer, D. T.; Sobkowiak, A.; Roberts, J. L. Electrochemistry for Chemists; Wiley: 1995.
- (40) You, Y.; Yao, H. R.; Xin, S.; Yin, Y. X.; Zuo, T. T.; Yang, C. P.; Guo, Y. G.; Cui, Y.; Wan, L. J.; Goodenough, J. B. Subzero-Temperature Cathode for a Sodium-Ion Battery. *Adv. Mater.* **2016**, 28, 7243–7248.
- (41) Wang, H.; Zhang, H.; Cheng, Y.; Feng, K.; Li, X.; Zhang, H. All-Nasicon LVP-LTP Aqueous Lithium Ion Battery with Excellent Stability and Low-Temperature Performance. *Electrochim. Acta* **2018**, 278, 279–289.
- (42) Tron, A.; Jeong, S.; Park, Y. D.; Mun, J. Aqueous Lithium-Ion Battery of Nano-LiFePO<sub>4</sub> with Antifreezing Agent of Ethyleneglycol for Low-Temperature Operation. *ACS Sustainable Chem. Eng.* **2019**, *7*, 14531–14538.
- (43) Ramanujapuram, A.; Yushin, G. Understanding the Exceptional Performance of Lithium-Ion Battery Cathodes in Aqueous Electrolytes at Subzero Temperatures. *Adv. Energy Mater.* **2018**, *8*, 1802624.
- (44) Nian, Q.; Wang, J.; Liu, S.; Sun, T.; Zheng, S.; Zhang, Y.; Tao, Z.; Chen, J. Aqueous Batteries Operated at -50 °C. *Angew. Chem., Int. Ed.* **2019**, 16994.
- (45) Dong, X.; Guo, Z.; Guo, Z.; Wang, Y.; Xia, Y. Organic Batteries Operated at -70° C. *Joule* **2018**, 2, 902–913.
- (46) Rustomji, C. S.; Yang, Y.; Kim, T. K.; Mac, J.; Kim, Y. J.; Caldwell, E.; Chung, H.; Meng, Y. S. Liquefied Gas Electrolytes for Electrochemical Energy Storage Devices. *Science* 2017, 356, eaal4263. (47) Lin, R.; Taberna, P.-L.; Fantini, S.; Presser, V.; Pérez, C. R.; Malbosc, F.; Rupesinghe, N. L.; Teo, K. B. K.; Gogotsi, Y.; Simon, P.

- Capacitive Energy Storage from -50 to 100 C Using an Ionic Liquid Electrolyte. J. Phys. Chem. Lett. 2011, 2, 2396-2401.
- (48) Duričković, I.; Claverie, R.; Bourson, P.; Marchetti, M.; Chassot, J. M.; Fontana, M. D. Water—Ice Phase Transition Probed by Raman Spectroscopy. *J. Raman Spectrosc.* **2011**, *42*, 1408–1412.
- (49) Beyer, K. D.; Hansen, A. R.; Poston, M. The Search for Sulfuric Acid Octahydrate: Experimental Evidence. *J. Phys. Chem. A* **2003**, *107*, 2025–2032.
- (50) Maynard-Casely, H. E.; Brand, H. E. A.; Wallwork, K. S. Structure and Thermal Expansion of Sulfuric Acid Octahydrate. *J. Appl. Crystallogr.* **2012**, *45*, 1198–1207.
- (51) Guo, Z.; Wang, T.; Wei, H.; Long, Y.; Yang, C.; Wang, D.; Lang, J.; Huang, K.; Hussain, N.; Song, C.; Guan, B.; Ge, B.; Zhang, Q.; Wu, H. Ice as Solid Electrolyte to Conduct Various Kinds of Ions. *Angew. Chem.* **2019**, 12699.
- (52) Wessells, C. D.; Peddada, S. V.; Huggins, R. A.; Cui, Y. Nickel Hexacyanoferrate Nanoparticle Electrodes for Aqueous Sodium and Potassium Ion Batteries. *Nano Lett.* **2011**, *11*, 5421–5425.
- (53) Wu, X.; Markir, A.; Xu, Y.; Zhang, C.; Leonard, D. P.; Shin, W.; Ji, X. A Rechargeable Battery with an Iron Metal Anode. *Adv. Funct. Mater.* **2019**, 29, 1900911.